

Cite this: *Chem. Sci.*, 2018, 9, 3508

Linking defects, hierarchical porosity generation and desalination performance in metal–organic frameworks†

Weibin Liang,^{‡a} Lin Li,^{‡b} Jingwei Hou,^{id *bc} Nicholas D. Shepherd,^a Thomas D. Bennett,^{id c} Deanna M. D'Alessandro^{*a} and Vicki Chen^{id b}

Composite membranes with defective metal–organic frameworks (MOFs) connect the emerging fields of MOF topological modification, MOF-polymer interfacial engineering and composite material functionalization. Although defective MOFs can be fabricated *via* thermal or chemical treatment, the relationship between hierarchical MOF structure and their performance in a polymeric membrane matrix has so far not been investigated. Here we show how a modulator fumarate-based MIL-53(Al) microwave synthesis process results in defective MOFs. This ligand replacement process leads to materials with hierarchical porosity, which creates a higher mesopore volume and Brønsted acidity without compromising the crystalline structure and pH stability. Compared with stoichiometric ratios, increasing the reaction time leads to more effective defect generation. The subsequent incorporation of defective MOFs into polyvinyl alcohol pervaporation membranes can effectively promote the fresh water productivity in concentrated brine treatment, with salt rejection of >99.999%. The membranes also have good long-term operational stability with effective antifouling behavior. We provide evidence that topological engineering of the MOF surface is related to their physical and chemical behaviors in a polymeric matrix, opening up the possibility of MOF defect engineering to realize selective separations, catalysis and sensing within a polymeric matrix.

Received 5th December 2017

Accepted 5th March 2018

DOI: 10.1039/c7sc05175a

rsc.li/chemical-science

1. Introduction

Metal–organic frameworks (MOFs) belong to a family of chemically and functionally diverse materials, which have attracted widespread interest across the areas of chemistry, biology, engineering and energy storage, to list but a few examples.^{1–4} In addition to new materials synthesis, recent research has gradually shifted towards exploring the physical, structural and chemical properties of materials which are already known.^{5,6} In particular, the engineering control of defects in MOF structures has been considered important in fine-tuning their properties for specific applications.^{7–9} Fundamentally, the crystalline structures of MOFs are based on a series of relatively weak interactions, *e.g.* coordination effects, hydrogen bonds, van der Waals' force, π – π interactions and so

on, which govern the exhibition of large-scale flexibility, structural disorder and both micro and macroscale defects. Modifying these interactions to facilitate missing ligands and metal ions, or metal reduction and displacement, rather than necessarily adverse effects, can endow MOF materials with specific functions, such as selective adsorption and improved catalytic activity.^{6,10–13}

'On top of' the microscopic defects within MOF structures, the generation of mesoporous defects with hierarchical porosity has attracted increasing attention.¹⁴ Essentially, the introduction of functionalized mesoporous structure on MOFs can be realized by controllable modification of coordinatively unsaturated metal sites.¹⁵ For example, the inclusion of monodentate synthetic modulators, *e.g.* acetic acid within synthetic routines, have been observed to generate 'spongy' networks of Fe³⁺ and Cr³⁺ based MOFs, or notably, frameworks with UiO-66 type structures.¹⁶ Another novel approach to construct the hierarchical structure on MOF is by using a nanosphere monolith template together a double-solvent-induced heterogeneous nucleation approach.¹⁷ There is, however, a fine balance between defect generation and loss of mechanical stability,^{18–20} and the advantageous functions of including defective MOFs within polymeric matrices such as membranes are poorly understood.

^aSchool of Chemistry, The University of Sydney, NSW 2006, Australia. E-mail: deanna.dalessandro@sydney.edu.au

^bUNESCO Center for Membrane Science and Technology, School of Chemical Engineering, The University of New South Wales, NSW 2052, Australia. E-mail: jingwei.hou@unsw.edu.au

^cDepartment of Materials Science and Metallurgy, University of Cambridge, Cambridge CB3 0FS, UK

† Electronic supplementary information (ESI) available. See DOI: 10.1039/c7sc05175a

‡ W. L. and L. L. contributed equally to this work.



In terms of membrane processes, the treatment of highly concentrated brine is technically challenging and energy demanding, as conventional pressure-driven filtration membrane is not a viable option due to the high osmotic pressure that must be overcome.²¹ The concentrated brine can also lead to rapid scaling and pore blocking for the membrane distillation process. Alternatively, membrane pervaporation is a promising technique, which has been extensively investigated for organic solvent separation and dehydration.²² The dense pervaporation membranes can effectively mitigate the scaling problem; but they still suffer from low desalination productivity and poor operational stability with brine feeds.²¹

An aluminum fumarate based MOF, MIL-53(Al) (also known as 'Basolite-100A') was selected as a possible candidate to link defect generation, hierarchical porosity and membrane performance due to (i) cost efficient synthesis in water with naturally earth abundant sources (fumaric acid and aluminum salts), (ii) high water adsorption capability with good thermal and chemical stability⁷ and (iii) the retention of initial pore structure upon pore evacuation, unlike the isostructural H₂BDC-based MIL-53 (BDC = 1,4-benzenedicarboxylate).²³ The framework has previously been studied for applications including natural gas storage, heat transformation and lithium-ion battery technology,^{7,23,24} but its potential to generate hierarchical structures has not been explored.

Herein, we investigated a controllable defect-generation technique for fumarate-based MIL-53(Al) MOFs (referred as MIL-53(Al) in the following text), drawing relationships between defect content and crystallinity, hierarchical structure and Brønsted acidity. The interaction between the hierarchically porous defective MOFs and polyvinyl (alcohol) (PVA) matrices was studied in the fabrication of nanocomposite pervaporation membranes. Finally, desalination membrane performance was examined with various complex feed solutions including model inland desalination brine, which is otherwise extremely difficult to process with other water treatment techniques.

2. Experimental section

2.1 Synthesis of MIL-53(Al)

Powdered MIL-53(Al)_{a,t min} ([Al(OH)(C₄H₂O₄)]) samples were synthesized using a microwave-assisted solvothermal method in an Anton Paar Monowave 300 microwave oven.^{25,26} For a general procedure, a 30 mL glass microwave vial was charged with Al₂(SO₄)₃·18H₂O (99.99%, Sigma-Aldrich), fumaric acid (99%, Sigma-Aldrich) and urea (≥99.5%, Ajax). Thereafter, Milli-Q water (18 MΩ) was introduced. The mixture was heated with magnetic stirring (600 rpm) to 130 °C within 1 min, and held at this temperature for a desired period of time before cooling to 55 °C within 2 min. The precipitates were vacuum filtered, and repeatedly washed with ethanol to remove the unreacted chemicals. The resulting powder was dried *in vacuo*. In this work, a series of different stoichiometric ratios (a) and reaction time (t, by default 30 min) were investigated for MIL-53(Al)_{a,t min} synthesis. Detailed information is given in the Section 3.1. A summary of the reaction conditions is provided in Table S1.†

2.2 X-ray powder diffraction (XRPD) and Le Bail cell simulation

XRPD measurements were performed on a PANalytical X'pert Pro diffractometer fitted with a solid-state PIXcel detector (45 kV, 40 mA, 1° divergence and anti-scatter slits, and 0.3 mm receiver and detector slits) using Cu-K_α (λ = 1.5406 Å) radiation. Profile fits were performed using the Le Bail extraction method in GSAS.²⁷

2.3 Potentiometric acid-base titration

Potentiometric titrations were conducted on a benchtop HANNA pH meter (HI2211-02, Basic pH and ORP Benchtop Meter) using procedures similar to those reported for Zr(OH)₄ and Zr/Hf-based MOFs.^{28–30} Prior to analysis, the pH meter was calibrated with commercial buffers (pH 4.00, 7.00, and 10.00, ProSource Scientific pH Buffer Calibration Standards). MOF samples were grounded with a mortar and pestle, and then approximate 50 mg of sample was dispersed in 50 mL of 0.01 M aq. NaNO₃ (≥99.0%, Sigma-Aldrich) solution, covered with Parafilm (Parafilm® M), and allowed to equilibrate for 5 h. The MOF suspension was then adjusted to pH 3 using 0.1 M aq. HCl (Merck) under magnetic stirring (1000 rpm) before being titrated with 0.1 M aq. NaOH (Merck) to pH 9.0–9.5. The injection rate of titrant was 20 μL every 30 s. Equivalence points were obtained from the first derivative of the resulting titration curves ($\frac{dpH}{dV_{0.1M NaOH}}$), where the inflection points in the derivative curve represent equivalence points. pK_a values were determined as the pH at one-half of the volume of titrant at the equivalence point. After titration, the MIL-53(Al) were filtered, washed with ethanol and dried *in vacuo* for XRPD analysis.

2.4 Characterization of MOFs

Attenuated total reflectance-Fourier transform infrared (ATR-FTIR) spectra were recorded for MIL-53(Al) on a PerkinElmer Spectrum Two IR spectrometer (with UATR Two attachment). TGA measurements were carried out on a DISCOVERY TGA Thermogravimetric Analyzer. Approximately 5 mg of each sample was placed on a platinum pan which was heated under a flow of air at a rate of 10 °C min^{−1} up to 700 °C. Field-emission SEM (FE-SEM) images were obtained using a Zeiss ULTRA plus microscope (working distance ~9 mm; acceleration voltage 20 kV). N₂ sorption isotherms were recorded on a 3Flex Surface Characterisation Analyser (Micromeritics Instruments Inc.).

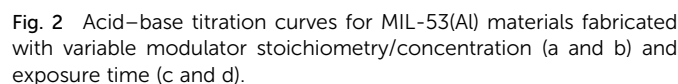
2.5 Pervaporation membrane fabrication

The composite pervaporation membrane was fabricated with a thin PVA surface coating on PVDF hollow fiber substrates. The substrate PVDF hollow fibre membrane was soaked in Milli-Q water overnight and left to dry at room temperature for at least 12 hours. 2 wt% of PVA was firstly dissolved in water, and then glutaraldehyde and methanol were added to the solution under constant stirring. The molar ratio of glutaraldehyde to PVA repeat unit is maintained at 0.2. To initiate the crosslinking reaction, HCl was added into the solution. A typical coating



and Photoshop, and eventually surface rendered with Cinema 4D from Maxon. The FIB-SEM samples contained 30 wt% of MOFs in PVA.

The Brønsted acidities of the MOF materials were studied *via* potentiometric titration.³⁸ Three acidic proton sources were generally observed, belonging to (1) water molecules situated in



the missing linker defect sites ($pK_a \approx 4.83$), (2) structural hydroxyl groups ($pK_a \approx 6.87$) and (3) hydroxyl groups stabilizing the MOF structures ($pK_a \approx 7.92$) (Fig. 2, Table 1, Fig. S3†). The lower pK_a values of the defective MOFs were indicative of a greater degree of structural hydroxyl groups and absorbed water molecules within their porous structures, consistent with the calculated molecular formula (Table 1). The emergence of a proton source within the defective MOFs aligns with our previous research with UiO-66.³⁹ For MIL-53(Al)₄ and MIL-53(Al)_{1,15 min}, protons from charge stabilization were not detected, possibly due to the detection limit of the instrument (Fig. S4†). PXRD recorded for MIL-53(Al) materials post-potentiometric analysis indicated that the crystallinity was unaffected under both acidic and basic conditions, as expected

Entry	TGA plateau ^a (@250 °C)	Approx. molecular formula	pK _{a1} μ-OH ₂ ^b	pK _{a2} μ ₃ -OH ^c	pK _{a3} μ-OH ^d	S _{BET} ^e (m ² g ⁻¹)	V _{total} ^f (cm ³ g ⁻¹)	V _{micro} ^g (cm ³ g ⁻¹)	V _{meso} ^h (cm ³ g ⁻¹)
MIL-53(Al) _{0.25}	145.3	[Al(OH) _{2.60} (C ₄ H ₂ O ₄) _{0.20}]	4.55	7.00	7.72	441.4(2)	0.56	0.02	0.55
MIL-53(Al) _{0.5}	152.5	[Al(OH) _{2.54} (C ₄ H ₂ O ₄) _{0.23}]	4.92	6.88	7.94	500.1(2)	0.43	0.15	0.31
MIL-53(Al) ₁	209.3	[Al(OH) _{2.02} (C ₄ H ₂ O ₄) _{0.49}]	4.88	7.11	7.92	907.6(6)	0.47	0.31	0.18
MIL-53(Al) ₂	243.2	[Al(OH) _{1.72} (C ₄ H ₂ O ₄) _{0.64}]	5.20	6.54	8.15	989.1(2)	0.54	0.30	0.22
MIL-53(Al) ₄	300.0	[Al(OH) _{1.22} (C ₄ H ₂ O ₄) _{0.89}]	4.71	7.15	—	1224.3(2)	0.51	0.46	0.06
MIL-53(Al) _{1,115 min}	289.7	[Al(OH) _{1.30} (C ₄ H ₂ O ₄) _{0.85}]	5.09	7.46	—	1213.5(2)	0.51	0.46	0.07
MIL-53(Al) _{1,45 min}	188.4	[Al(OH) _{2.20} (C ₄ H ₂ O ₄) _{0.40}]	4.75	6.72	7.88	801.5(2)	0.63	0.20	0.45
MIL-53(Al) _{1,60 min}	119.6	[Al(OH) _{2.82} (C ₄ H ₂ O ₄) _{0.09}]	4.54	6.10	7.89	426.9(2)	0.77	0.01	0.78

^a Data was taken from the normalized aerobic TGA data. ^b $\mu\text{-OH}_2$ = water molecules in missing linker defect sites. ^c $\mu_3\text{-OH}$ = structural hydroxyl group. ^d $\mu\text{-OH}$ = hydroxyl groups present for charge stabilization. ^e Calculated from the N_2 adsorption isotherms measured at 77 K. Values in parentheses indicate the uncertainties. ^f V_{total} represents total pore volume determined using the adsorption branch of the 77 K N_2 isotherms at $p/p_0 = 0.99$. ^g V_{micro} represents the specific micropore volume calculated using the t -plot method. ^h V_{meso} represents the specific mesopore volume calculated from the N_2 adsorption isotherm using the BJH method.



Fig. 3 SEM images for MIL-53(Al) materials at high magnification (40 K magnification).

based on structural robustness associated with frameworks in general, even after the defects generation (Fig. S5†).

The mesoporous structures of the series of MIL-53(Al)_{a,t min} materials were visualized by scanning electron microscopy (SEM, Fig. 3 and S6†), with pore apertures found to lie within the 20–500 Å literature range,⁴⁰ the latter being particularly pronounced in MIL-53(Al)_{0.25}, MIL-53(Al)_{0.5}, MIL-53(Al)_{1.45 min} and MIL-53(Al)_{1.60 min}. As these materials are subject to substantial modulator exposure and/or dilution during assembly, the presence of mesopores in the structures is consistent with the aforementioned effects from urea and concentration, as well as previous characterization results (ATR-FTIR, TGA and acid–base titration). This demonstrates the capacity of this technique in tuning the architectural structure of MOFs.⁴¹ The introduction of mesoporosity was further

substantiated by 77 K N₂ isotherms (Fig. 4a–d, S7–S22†). Type I physisorption curves were observed for all samples, with H₄ hysteresis observed for MIL-53(Al) materials, in accordance with the presence of mesoporosity.⁴² The calculated micro- and mesopore profiles (V_{meso} and V_{micro}) for the MIL-53(Al) series (Fig. 4e–f, Table 1) demonstrate increased mesoporosity with increasing reaction time and urea concentration, although an inverse relationship is noted in for S_{BET} and V_{micro} with respect to missing linker defects generated, as reported previously in the MOF literature.^{43–48}

At low to medium partial pressures, the water molecules physically adsorb to the surface and within micropores of the material, while at high partial pressure conditions the adsorption mainly occurs within the mesoporous structures, forming a large amount of water clusters *via* hydrogen bonds.^{49,50}

3.2 Fabrication of MIL-53/PVA composite membranes

The MIL-53(Al) samples fabricated with different reaction times were applied for composite pervaporation membrane fabrication. MOF materials were blended into PVA and then coated onto a PVDF hollow fiber surface (Fig. 5a). Compared with pure PVA coating, which has a smooth morphology with a consistent thickness of 0.8 μm, the incorporation of MOFs generated hierarchical roughness on the membrane surface, without a significant increase of the selective layer thickness (Fig. S23†). Energy dispersive X-ray spectroscopy (EDX) mapping results confirmed the presence of MIL-53(Al) within the selective layers (Fig. S24†), although agglomeration occurred with particularly high loadings. Compared with the PVA/PVDF composite hollow

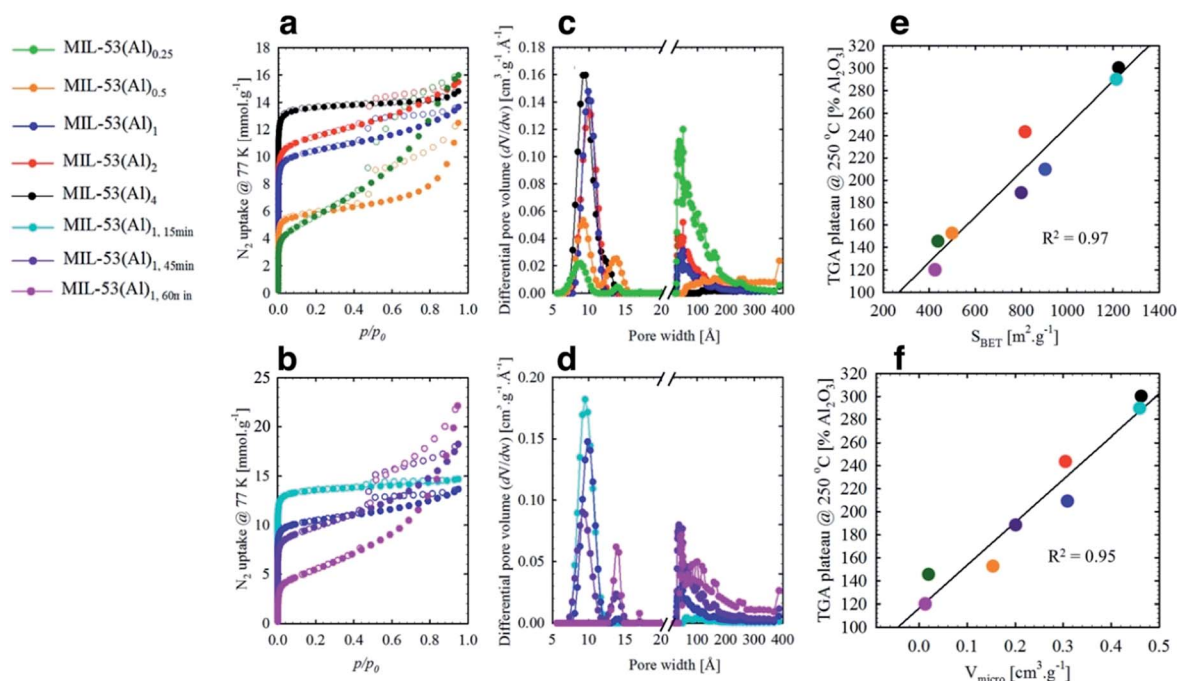


Fig. 4 N₂ isotherms (77 K) and pore size distributions for MIL-53(Al) materials with adjusted modulator stoichiometry/concentration (a and c) and varied reaction time (b and d); linear fits obtained by plotting (e) the BET surface areas (S_{BET}) and (f) micro pore volume (V_{micro}) of all 8 samples against their respective TGA plateau at 250 °C.

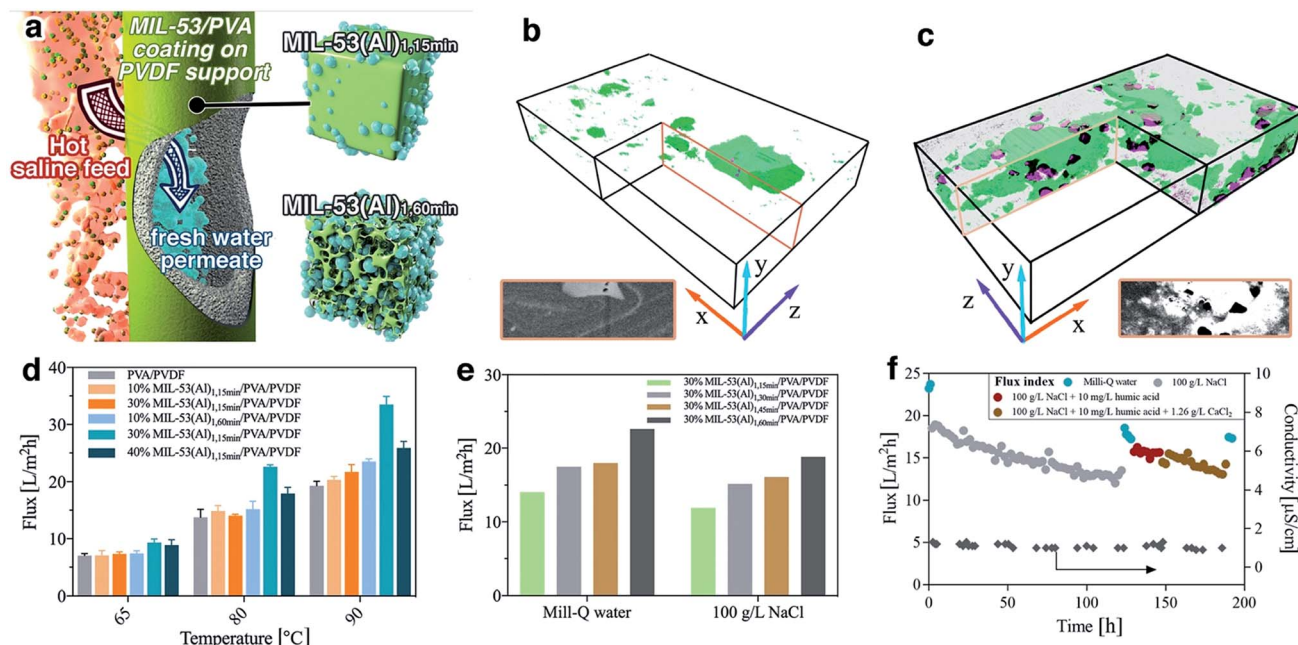


Fig. 5 (a) Schematic diagram of the nanocomposite pervaporation membrane for brine treatment; (b, c) surface-rendered views of the segmented FIB-SEM tomograms for mixed matrix membranes containing (b) MIL-53(Al)_{1.15 min} and (c) defective type MIL-53(Al)_{1.60 min} in PVA matrix. MOF particles are shown in green, while voids are shown in purple. The dimensions of the boxes shown in (b) and (c) along the $x : y : z$ directions are 9.25, 1.5 and 5.0 μm , respectively. The insert are reference SEM images for the highlighted cross-sectional area; (d, e) pervaporation flux for different membranes. All reported values were the averaged flux of 4 hours' operation after initial stabilisation. (d) Milli-Q water was used as feed. (e) Feed solution temperature was 80 °C. For clarity, MIL-53(Al)₁ was denoted as MIL-53(Al)_{1.30 min} in this graph; (f) long term desalination performance with the complex brine feeds at 80 °C using 30% MIL-53(Al)_{1.60 min}/PVA/PVDF membrane.

fiber, the membrane with MIL-53(Al) exhibited improved mechanical properties, indicating a good composition between PVA and fillers (Fig. S25†).

Given the long-standing issues of mixed matrix membrane compatibility between polymeric matrix and nanofillers, a series of free-standing MIL-53(Al)/PVA films were synthesized in order to probe the interface between MIL-53(Al) nanofiller and the polymeric PVA matrix. FTIR results demonstrated a shift to lower wavenumber of the OH stretching band in the PVA membrane, indicating the potential formation of hydrogen bonds as well as higher water adsorption within the film (Fig. S26†).⁵¹ We further examined the water uptake capability for the film (Table S3†). The addition of MIL-53(Al)_{1.15 min} had a negligible improvement on the water adsorption, indicating that the surface OH groups of nanofillers are mostly occupied by the polymeric matrix forming hydrogen bonds. The creation of large scale mesoporous voids in the nanofillers however, e.g. MIL-53(Al)_{1.60 min}, resulted in promotion of water uptake in the films. Such observations are aligned with the glass transition (T_g) shift for PVA films (Fig. S27†), where the T_g is raised by hydrogen bond formation and lowered by water-induced polymer swelling.^{52,53} More specifically, the pure PVA has a T_g of 63 °C which is comparable to the reference values.⁵³ However, T_g for some film samples were too weak/or too broad to be detected, or they are suppressed due to polymer chain confinement. The incorporation of MIL-53(Al)_{1.15 min} can form hydrogen bond with PVA chains, leading to an improved T_g . In comparison, the addition of defective MOFs can improve the water uptake for the

film, leading to PVA chain swelling and subsequently reduced T_g . The presence of crystalline MIL-53(Al) within PVA film was further confirmed by the TGA and XRD results (Fig. S28–S29†).

The internal structure and filler-matrix interfacial morphology of the mixed matrix films were further studied with tomographic focused ion beam scanning electron microscopy (FIB-SEM). A trench was carved on the top surface and a series of SEM images were recorded of cross-sectional directions, and then the surface rendered views after segmentation of different phases (Fig. 5b–c and S30†). The full tomograms are provided as ESI Movies 1 and 2.† Significant differences in the microscale structures were observed: the defective MOF leaves a significant fraction of the composite materials unoccupied, due to their mesoporous structures.

3.3 Nanocomposite membrane pervaporation performance

To further study their technical relevance, the MOF-PVA nanocomposite hollow fiber membranes were tested for their pervaporation performance (Scheme S1†). As shown in Fig. 5d, when using Milli-Q water as feed, the incorporation of MIL-53_{1.15 min} (containing fewer defects) into PVA has a negligible effect on the permeation flux as compared with a PVA benchmark membrane. This observation aligns with the above water uptake results. By comparison, the beneficial role of defective MOF (MIL-53_{1.60 min}) is immediately apparent with improved water flux. This result is illustrative of the encouraging water transport efficiency for the composite membranes:

4. Conclusion

Conflicts of interest

Acknowledgements

Notes and references

- This journal is © The Royal Society of Chemistry 2018

- M. Muhler and R. A. Fischer, *Angew. Chem., Int. Ed.*, 2014, **53**, 7058–7062.
- 7 E. Alvarez, N. Guillou, C. Martineau, B. Bueken, B. Van de Voorde, C. Le Guillouzer, P. Fabry, F. Nouar, F. Taulelle, D. de Vos, J.-S. Chang, K. H. Cho, N. Ramsahye, T. Devic, M. Daturi, G. Maurin and C. Serre, *Angew. Chem., Int. Ed.*, 2015, **54**, 3664–3668.
- 8 D. S. Sholl and R. P. Lively, *J. Phys. Chem. Lett.*, 2015, **6**, 3437–3444.
- 9 Z. Fang, B. Bueken, D. E. De Vos and R. A. Fischer, *Angew. Chem., Int. Ed.*, 2015, **54**, 7234–7254.
- 10 T.-H. Park, A. J. Hickman, K. Koh, S. Martin, A. G. Wong-Foy, M. S. Sanford and A. J. Matzger, *J. Am. Chem. Soc.*, 2011, **133**, 20138–20141.
- 11 J. Canivet, M. Vandichel and D. Farrusseng, *Dalton Trans.*, 2016, **45**, 4090–4099.
- 12 Y. Liu, R. C. Klet, J. T. Hupp and O. Farha, *Chem. Commun.*, 2016, **52**, 7806–7809.
- 13 F. Vermoortele, B. Bueken, G. Le Bars, B. Van de Voorde, M. Vandichel, K. Houthoofd, A. Vimont, M. Daturi, M. Waroquier, V. Van Speybroeck, C. Kirschhock and D. E. De Vos, *J. Am. Chem. Soc.*, 2013, **135**, 11465–11468.
- 14 G. Cai and H.-L. Jiang, *Angew. Chem.*, 2017, **129**, 578–582.
- 15 Z. Fang, J. P. Dürholt, M. Kauer, W. Zhang, C. Lochenie, B. Jee, B. Albada, N. Metzler-Nolte, A. Pöpl, B. Weber, M. Muhier, Y. Wang, R. Schmid and R. A. Fischer, *J. Am. Chem. Soc.*, 2014, **136**, 9627–9636.
- 16 B. Bueken, N. Van Velthoven, T. Willhammar, T. Stassin, I. Stassen, D. A. Keen, G. V. Baron, J. F. M. Denayer, R. Ameloot, S. Bals, D. De Vos and T. D. Bennett, *Chem. Sci.*, 2017, **8**, 3939–3948.
- 17 K. Shen, L. Zhang, X. Chen, L. Liu, D. Zhang, Y. Han, J. Chen, J. Long, R. Luque, Y. Li and B. Chen, *Science*, 2018, **359**, 206–210.
- 18 A. W. Thornton, R. Babarao, A. Jain, F. Trouselet and F. X. Coudert, *Dalton Trans.*, 2016, **45**, 4352–4359.
- 19 M. J. Cliffe, E. Castillo-Martínez, Y. Wu, J. Lee, A. C. Forse, F. C. N. Firth, P. Z. Moghadam, D. Fairen-Jimenez, M. W. Gaultois, J. A. Hill, O. V. Magdysyuk, B. Slater, A. L. Goodwin and C. P. Grey, *J. Am. Chem. Soc.*, 2017, **139**, 5397–5404.
- 20 M. J. Cliffe, J. A. Hill, C. A. Murray, F.-X. Coudert and A. L. Goodwin, *Phys. Chem. Chem. Phys.*, 2015, **17**, 11586–11592.
- 21 L. Li, J. Hou, Y. Ye, J. Mansouri and V. Chen, *Desalination*, 2017, **422**, 49–58.
- 22 Y.-H. Deng, J.-T. Chen, C.-H. Chang, K.-S. Liao, K.-L. Tung, W. E. Price, Y. Yamauchi and K. C. W. Wu, *Angew. Chem., Int. Ed.*, 2016, **55**, 12793–12796.
- 23 Y. Wang, Q. Qu, G. Liu, V. S. Battaglia and H. Zheng, *Nano Energy*, 2017, **39**, 200–210.
- 24 P. G. Yot, L. Vanduyfhuys, E. Alvarez, J. Rodriguez, J.-P. Itie, P. Fabry, N. Guillou, T. Devic, I. Beurroies, P. L. Llewellyn, V. Van Speybroeck, C. Serre and G. Maurin, *Chem. Sci.*, 2016, **7**, 446–450.
- 25 E. Alvarez, N. Guillou, C. Martineau, B. Bueken, B. Van de Voorde, C. Le Guillouzer, P. Fabry, F. Nouar, F. Taulelle, D. de Vos, J.-S. Chang, K. H. Cho, N. Ramsahye, T. Devic, M. Daturi, G. Maurin and C. Serre, *Angew. Chem., Int. Ed.*, 2015, **54**, 3664–3668.
- 26 W. Liang, R. Babarao, T. L. Church and D. M. D'Alessandro, *Chem. Commun.*, 2015, **51**, 11286–11289.
- 27 A. Altomare, M. C. Burla, M. Camalli, B. Carrozzini, G. L. Casciarano, C. Giacovazzo, A. Guagliardi, A. G. G. Moliterni, G. Polidori and R. Rizzi, *J. Appl. Crystallogr.*, 1999, **32**, 339–340.
- 28 R. C. Klet, Y. Liu, T. C. Wang, J. T. Hupp and O. K. Farha, *J. Mater. Chem. A*, 2016, **4**, 1479–1485.
- 29 T. J. Bandosz, M. Laskoski, J. Mahle, G. Mogilevsky, G. W. Peterson, J. A. Rossin and G. W. Wagner, *J. Phys. Chem. C*, 2012, **116**, 11606–11614.
- 30 T. G. Glover, G. W. Peterson, J. B. DeCoste and M. A. Browe, *Langmuir*, 2012, **28**, 10478–10487.
- 31 J. Oomens and J. D. Steill, *J. Phys. Chem. A*, 2008, **112**, 3281–3283.
- 32 S. Pradhan, V. Sahu and B. G. Mishra, *J. Mol. Catal. A: Chem.*, 2016, **425**, 297–309.
- 33 K. A. Fisher, J. J. Meisinger and B. R. James, *J. Environ. Qual.*, 2016, **45**, 349–359.
- 34 L. Valenzano, B. Civalieri, S. Chavan, S. Bordiga, M. H. Nilsen, S. Jakobsen, K. P. Lillerud and C. Lamberti, *Chem. Mater.*, 2011, **23**, 1700–1718.
- 35 J. Oomens and J. D. Steill, *J. Phys. Chem. A*, 2008, **112**, 3281–3283.
- 36 P. J. Larkin, *Infrared and Raman Spectroscopy; Principles and Interpretation*, Elsevier, 2011.
- 37 J.-S. Choi, W.-J. Son, J. Kim and W.-S. Ahn, *Microporous Mesoporous Mater.*, 2008, **116**, 727–731.
- 38 R. C. Klet, Y. Liu, T. C. Wang, J. T. Hupp and O. K. Farha, *J. Mater. Chem. A*, 2016, **4**, 1479–1485.
- 39 W. Liang, C. J. Coghlán, F. Ragon, M. Rubio-Martínez, D. M. D'Alessandro and R. Babarao, *Dalton Trans.*, 2016, **45**, 4496–4500.
- 40 Z. Liu, N. Fujita, K. Miyasaka, L. Han, S. M. Stevens, M. Suga, S. Asahina, B. Slater, C. Xiao, Y. Sakamoto, M. W. Anderson, R. Ryoo and O. Terasaki, *Microscopy*, 2013, **62**, 109–146.
- 41 R. Semino, N. A. Ramsahye, A. Ghoufi and G. Maurin, *Microporous Mesoporous Mater.*, 2017, **254**, 184–191.
- 42 M. Thommes, K. Kaneko, A. V. Neimark, J. P. Olivier, F. Rodriguez-Reinoso, J. Rouquerol and K. S. W. Sing, Physisorption of gases, with special reference to the evaluation of surface area and pore size distribution (IUPAC Technical Report), *Pure Appl. Chem.*, 2015, 1051.
- 43 O. V. Gutov, M. G. Hevia, E. C. Escudero-Adán and A. Shafir, *Inorg. Chem.*, 2015, **54**, 8396–8400.
- 44 D. Wu, W. Yan, H. Xu, E. Zhang and Q. Li, *Inorg. Chim. Acta*, 2016, **460**, 93–98.
- 45 K. Wang, C. Li, Y. Liang, T. Han, H. Huang, Q. Yang, D. Liu and C. Zhong, *Chem. Eng. J.*, 2016, **289**, 486–493.
- 46 C. Atzori, G. C. Shearer, L. Maschio, B. Civalieri, F. Bonino, C. Lamberti, S. Svelle, K. P. Lillerud and S. Bordiga, *J. Phys. Chem. C*, 2017, **121**, 9312–9324.



- 47 G. C. Shearer, J. G. Vitillo, S. Bordiga, S. Svelle, U. Olsbye and K. P. Lillerud, *Chem. Mater.*, 2016, **28**, 7190–7193.
- 48 G. C. Shearer, S. Chavan, S. Bordiga, S. Svelle, U. Olsbye and K. P. Lillerud, *Chem. Mater.*, 2016, **28**, 3749–3761.
- 49 B. Bozbiyik, J. Lannoeie, D. E. De Vos, G. V. Baron and J. F. M. Denayer, *Phys. Chem. Chem. Phys.*, 2016, **18**, 3294–3301.
- 50 J. A. Coelho, A. M. Ribeiro, A. F. P. Ferreira, S. M. P. Lucena, A. E. Rodrigues and D. C. S. d. Azevedo, *Ind. Eng. Chem. Res.*, 2016, **55**, 2134–2143.
- 51 Z. H. Ping, Q. T. Nguyen, S. M. Chen, J. Q. Zhou and Y. D. Ding, *Polymer*, 2001, **42**, 8461–8467.
- 52 J. Rault, R. Gref, Z. H. Ping, Q. T. Nguyen and J. Néel, *Polymer*, 1995, **36**, 1655–1661.
- 53 K. E. Strawhecker and E. Manias, *Chem. Mater.*, 2000, **12**, 2943–2949.

